Anthropogenic Influence on the Diurnal Temperature Range since 1901

CHUNHUI LU,[a] YING SUN,[a,b] AND XUEBIN ZHANG[c]

[a] *National Climate Center, Laboratory for Climate Studies, China Meteorological Administration, Beijing, China*
[b] *Collaborative Innovation Center on Forecast and Evaluation of Meteorological Disasters (CIC-FEMD), Nanjing University of Information Science and Technology, Nanjing, China*
[c] *Climate Research Division, Environment and Climate Change Canada, Toronto, Canada*

(Manuscript received 2 December 2021, in final form 14 June 2022)

ABSTRACT: The diurnal temperature range (DTR) as measured by the difference between daily maximum (Tmax) and minimum (Tmin) temperatures is of great importance to human health, ecology, and agriculture. The link of its long-term change to anthropogenic forcing is still unclear. This study shows evidence of human influence on long-term changes in DTR over the globe, five continents, and China during the past century (1901–2014). Using multiple observational datasets, we find a general decrease in the DTR over most of the global land since 1901, especially after the mid-1950s. Changes in DTR are due to different warming rates of Tmax and Tmin in response to external forcings. The climate models that participated in phase 6 of the Coupled Model Intercomparison Project Phase 6 (CMIP6) generally reproduce most of the changes in DTR, along with those in Tmax and Tmin. The models have underestimated the observed changes in DTR, however. A formal detection and attribution analysis shows that the anthropogenic forcing signal, including both greenhouse gas and aerosol emissions but dominated by the greenhouse gas emissions, is the main driver for these changes. The anthropogenic aerosol signal can be detected in Tmax and Tmin but not in DTR during the period of 1901–2014 over the globe and most continents. These indicate the observed decrease in DTR is not a simple response to anthropogenic aerosol emission. The natural signal is negligible in almost all the cases. Globally, anthropogenic influence is estimated to explain more than 90% of the observed changes in the three variables. In China, human influence is also clearly detected, although model simulated results on the regional scale have larger deviation.

SIGNIFICANCE STATEMENT: The diurnal temperature range (DTR) is of great importance in many areas. We compare multiple observational datasets with the simulations by climate models that participated in the latest phase (phase 6) of the Coupled Model Intercomparison Project (CMIP6), finding evidence of human influence on long-term changes in DTR over the past century (1901–2014) and robust evidence for the period since the early 1950s. The decrease in DTR as seen in the observational dataset is caused by different warming rates of daily maximum and daily minimum temperature in response to anthropogenic forcing, including both greenhouse gases and aerosols.

KEYWORDS: Anthropogenic effects/forcing; Climate change; Climatology

1. Introduction

Diurnal temperature range (DTR), the difference between daily maximum (Tmax) and minimum (Tmin) temperatures, is important to human health, ecology, and agriculture. Changes in DTR can affect parasite infection and the rate of parasite development (Paaijmans et al. 2010), lead to divergent responses of vegetation growth and carbon sequestration (Peng et al. 2013), alter carbon trade-off (photosynthesis vs respiration), and affect agricultural productivity (Sunoj et al. 2020). The Tmax usually occurs a few hours after maximum solar radiation appears, when the boundary layer has been completely mixed. The Tmin tends to occur around dawn when surface radiative cooling is drawing to an end, and atmospheric vertical stratification is becoming more and more stable. DTR is an important indicator of climate system, providing additional dimension of information to mean temperature (Braganza et al. 2004). Trends and variability in DTR also have implications for understanding the changes in stratification propensity and the deeper boundary layer dynamics (Christy et al. 2009; Steeneveld et al. 2011; McNider et al. 2012). For example, changes in DTR also have potential applicability to distinguish influences on temperature between longwave and shortwave radiation (Jackson and Forster 2013; Wang and Dickinson 2013).

Studies since the early 1990s have shown a decrease in DTR on the global scale and on regional scales in many regions (e.g., Karl et al. 1993; Easterling et al. 1997; Alexander et al. 2006; Wang and Dillon 2014; Thorne et al. 2016a); the magnitude of the observed changes in DTR is much smaller than that of mean temperature. There was large uncertainty in DTR trend estimates, leading to a medium confidence in the Fourth and the Fifth Assessments of the Intergovernmental Panel on Climate Change (IPCC; Trenberth et al. 2007;

Denotes content that is immediately available upon publication as open access.

Supplemental information related to this paper is available at the Journals Online website: https://doi.org/10.1175/JCLI-D-21-0928.s1.

Corresponding author: Ying Sun, sunying@cma.gov.cn

DOI: 10.1175/JCLI-D-21-0928.1

Hartman et al. 2013). But a comparison of a wide range of datasets showed agreement in a global decrease in DTR since the 1950s among datasets, with most of the decrease appearing over 1950–80, although estimated changes for the pre-1950 period were more uncertain, in large part because of the sparse data network (Thorne et al. 2016b). A subsequent study based on a different dataset confirmed these results (Sun et al. 2018).

The decrease of DTR is a result of asymmetric warming in Tmin and Tmax (Karl et al. 1993). The causes of this asymmetric warming have been studied from the perspective of external forcing such as greenhouse gases, aerosols, and land use and land cover changes (Zhou et al. 2010; Lewis and Karoly 2013; Liu et al. 2016; Christidis and Stott 2016), and from the perspective of physical mechanisms in response to external forcings including longwave and shortwave radiation, cloudiness, precipitation, and soil moisture (e.g., Dai et al. 1999; Stone and Weaver 2003; Stjern et al. 2020). Many studies did not make a clear distinction between direct radiative effect of external forcings and the secondary effect of climate responses to external forcing such as through the changes in soil moisture and precipitation. Overall, both greenhouse gases (GHGs) and aerosols seem to result in a decrease in DTR. Zhou et al. (2010) compared multimodel simulations with observations, finding that "decreased surface downward shortwave radiation due to increasing aerosols and water vapor contributes most to the decreases in DTR in the models" (p. 1289). Here, the role of aerosols in reducing DTR was made explicit, although the role of greenhouse gases was only implicitly mentioned through the increase of water vapor, which is a result of warming. The observed decrease in DTR over Asia was reproduced by climate models under the combined effect of anthropogenic and natural forcing, with GHG forcing produced larger decrease in DTR for Asia overall. While understanding physical mechanisms involved in the observed decrease in DTR is useful, quantifying influence of external forcing on DTR is very important for our confidence about past changes as well as future projections. Yet, a clear quantification of contribution to the observed decrease in DTR by external forcings is generally lacking.

Detection and attribution analyses have played a vital role in establishing human influence on climate (Mitchell et al. 2001; Hegerl et al. 2007; Bindoff et al. 2013; Eyring et al. 2021). Using the optimal fingerprint detection method, analyses have shown clear human influences on the mean temperature on global (Tett et al. 2002; Stott et al. 2001, 2006; Zhang et al. 2006; Jones et al. 2013; Hegerl et al. 2019; Gillett et al. 2021) and on continental and regional scales (Stott 2003; Zwiers and Zhang 2003), and on various aspects of temperature extremes (Zwiers et al. 2011; Min et al. 2013; Kim et al. 2015; Morak et al. 2013; Lu et al. 2016, 2018; Christidis and Stott 2016). Confidence about human influence on climate has become so high that the IPCC in its most recent assessment stated that "It is unequivocal that human influence has warmed the atmosphere, ocean and land since pre-industrial times" (Eyring et al. 2021, p. 425). While confidence about human influence on many variables, especially those related to mean and extreme temperatures, is very high, the detection and attribution of human influence on other variables is still very challenging owing to the limitations in the quality and availability of observational data and relatively weak strength of signals.

Detection and attribution analysis of observed changes in DTR has been limited. We are aware of one study that conducted a formal detection and attribution analysis on DTR (Christidis and Stott 2016) so far. In this study, the authors analyzed the influence of external forcing on DTR and other 15 temperature indices for global land and Europe. They compared observational HadEX2 data (Donat et al. 2013) with those simulated by the Hadley Centre's Earth System model HadGEM2-ES (Jones et al. 2011) for 1960–2010 and they did not detect evidence of external forcing on DTR. With a better understanding of observational data quality and extended sample size, and availability of simulations of multiple ensembles that by models participated in phase 6 of the Coupled Model Intercomparison Project (CMIP6; Eyring et al. 2016) we attempt to fill in this gap by revisiting detection and attribution analysis of observed changes in DTR over the past century. Because of uncertainty in observational data over the first half of the twentieth century, we also conducted analyses excluding that portion of the data. In the paper, we first compare changes of DTR in different periods based on multiple observational datasets. We then compare the observed changes with those simulated by CMIP6 models. We use an optimal fingerprint method to investigate the contribution of external forcings to observed changes in DTR. As models underestimate the observed changes in DTR, we also conducted detection and attribution analysis on mean Tmax and Tmin in a hope that this might shed some light about the sources of the underestimation. We include China (CN) as a separate region because of our strong interest in the country. The remaining of the paper is structured as follows: section 2 describes the datasets and detection methods, including the steps of data processing; section 3 shows the temporal and spatial variations in DTR, and presents the detection and attribution results; the conclusions are given in section 4 along with some discussion.

2. Data and methods

a. *Observations*

The DTR is defined as the difference between daily maximum and daily minimum temperatures (Zhang et al. 2011), and here we use the annual mean results calculated from the daily or monthly values for further analysis. We consider changes in the DTR on global and continental scales by including the global land and five continental regions: Europe (EUR), Asia (ASI), North America (NAM), South America (SAM), and Australia (AUS) as defined in Jones et al. (2013). Africa is not included in this study because of poor data availability. We consider the period starting from the end of the preindustrial era. Because CMIP6 historical simulations generally stop at 2014, the time period used in the study is 1901–2014. Because of known data quality and homogeneity issues (Thorne et al. 2016b), we also analyzed the data for 1951–2014.

TABLE 1. A list of multimodel simulations used in this study. Numbers in the columns for ALL, NAT, GHG, AA, and SSP indicate ensemble sizes, and those in the columns CTL-114 and CTL-64 are the number of 114- or 64-yr chunks of the control simulations.

Model name	ALL	CTL-114	CTL-64	NAT	GHG	AA	SSP2–4.5
BCC-CSM2-MR	3			3	3	3	1
CanESM5	25	6	11	10	10	10	10
CNRM-ESM2-1		4	7				
CNRM-CM6-1	9	4	7	3	3	3	1
EC-Earth3		4	7				
EC-Earth3-Veg		1	4				
GFDL-CM4_gr2		4	7				
GFDL-CM4		4	7				
GFDL-ESM4		4	7				
HadGEM3-GC31-LL	4	4	7	4	4	4	1
IPSL-CM6A-LR	6	10	18	6	6	6	6
INM-CM4-8		4	7				
MIROC6		4	7				
MRI-ESM2-0	3	1	2	3	3	3	1
MIROC-ES2L		4	7				
MPI-ESM1-2-HR		4	7				
NorESM2-LM	3	1	2	3	3	3	
UKESM1-0-LL		1	2				
SUM (models)	53 (7)	64 (17)	116 (17)	32 (7)	32 (7)	32 (7)	20 (6)

There exist multiple observational DTR datasets. There can be substantial ambiguity in estimated DTR changes prior to 1950 due to changes in data coverage, but the estimated changes since 1951 to date among different datasets are similar (Thorne et al. 2016b; Sun et al. 2018). We used three datasets in this study: the high-resolution gridded temperature from the Climatic Research Unit (CRU, v4.05) at the University of East Anglia (Harris et al. 2014), the Berkeley Earth Surface Temperature product (Rohde et al. 2012, 2013), and the China Meteorological Administration global Land Surface Air Temperature (CLSAT; Xu et al. 2018). These datasets were selected because they provide DTR, Tmin, and Tmax and because they were created by three types of groups: a group that is known for creating global temperature datasets for a long time, an independent group, and a group new to the creation of a global temperature dataset. Both Berkley and CLSAT data are anomalies relative to 1961–90. They are on 1° × 1° and 5° × 5° grids, respectively. The Berkeley data are regridded onto the 5° × 5° grid to be consistent with CLAST. The CRU data are anomalies relative to 1901–30 and 1961–90. They are also regridded onto the 5° × 5° grids. The anomalies relative to 1961–90 are used to compare three datasets, and anomalies relative to 1901–30 are used for the detection and attribution analysis. The gridded data are used to estimate regional-mean DTR based on area weighting. Regional trends are estimated based on the regional mean series.

Daily maximum and daily minimum temperatures from 2419 Chinese stations (CN-2419) are also used to compare and analyze changes in the DTR in China. These data cover the period from 1951 to 2018 and have been quality controlled and homogeneity adjusted (Xu et al. 2013) by the China National Meteorological Information Center. The temperature anomalies (relative to 1961–90 average) at each station are aggregated to produce gridded datasets at the 5° × 5° resolution, consistent with other observational datasets. When we perform the detection and attribution analysis on China, we use the values on the grids where both CRU and CN-2419 have values.

b. *Model simulations*

Daily DTR values are computed as the difference between daily Tmax and Tmin of relevant model outputs. These values are averaged annually and used in the subsequent analyses. We use output from the simulations under the following forcings: the combined effect of anthropogenic and natural external forcing (ALL), natural external forcing (NAT), greenhouse gas forcing (GHG) and anthropogenic aerosol forcing (AA) over the period of 1850–2014. These simulations are used to estimate model responses during different study periods. The simulations under the Shared Socioeconomic Pathway SSP2–4.5 scenarios for 2015–2100 are also used to estimate future changes of DTR. We use the preindustrial control (CTL) simulations from 17 models to and intra-ensemble difference of the forced runs to estimate the internal climate variability needed in the detection and attribution analyses. The control simulations are divided into 64- and 114-yr chunks corresponding to the lengths of analyses periods (1901–2014 and 1951–2014). Table 1 lists the models, the ensemble sizes, and the number of control simulation chunks. Anomaly values of Tmax, Tmin, and DTR (relative to 1901–30) from the model simulations are first computed on the model's native grid and then bilinearly interpolated onto the 5° × 5° grid of the observational data. The model outputs are masked to mimic observational data availability. These masked data are averaged using area weighting to obtain global and continental and regional mean values. When computing multimodel ensemble mean, we give equal weight to each model by first computing the ensemble mean for individual model and then averaging them across the models.

c. Detection methods

We use a multivariate linear regression model $Y = (X - \gamma)\beta + \varepsilon$ (Allen and Stott 2003) to regress the observation onto the modeled responses to external forcings X, also known as the signals. The regression coefficients or estimated scaling factors β adjust the signals X and provide a best match with the observations Y; also, γ represents the noise in the signals estimates of multimodel ensemble mean and ε is the regression residual representing natural internal variability of the climate. The estimation is based on the regularized methods of Ribes et al. (2013). A residual consistency test is conducted using the implementation of Ribes and Terray (2013). Detection of a signal is claimed if the 5th percentile of the corresponding scaling factor is above zero. Moreover, if the 90% range for a scaling factor lies entirely above zero and includes unity simultaneously, the observed changes are estimated to be consistent with the response of the corresponding forcing leading to attribution. When β is larger than 1, it indicates underestimation in modeled response of the corresponding signal.

To make the noise covariance matrix full rank, as needed for the detection and attribution analyses, nonoverlapping 5-yr mean series are applied to reduce the temporal dimension. The 5-yr mean values are considered as a compromise between reducing the internal variability and maintaining sufficient responses to short-term natural external forcings such as volcanic eruption. Regional means are used rather than grid cell series to reduce the spatial dimension. Thus, for the respective detection analysis of the global land, each continent, and China, the number of dimensions is 23 for the period of 1901–2014, made up of 22 nonoverlapping 5-yr means and one additional 4-yr mean. Similarly, the number of dimensions is 13 when the study period is 1951–2014. The last data point is also the average over a 4-yr period (2011–14). For the global analysis, we also considered spatial-temporal analysis by combining the regional time series from five continents (Africa is not included) as five spatial dimensions (GLB_com). This approach has a potential to improve detectability of signals if climate responses differ across the space (Hu et al. 2020). The available control runs and within-ensemble difference data were equally split into two independent sets. Then these two sets were used for optimization to calculate the best estimate of scaling factor β, estimate the uncertainty range of β, and perform the residual consistency test.

Three types of regression analyses are conducted, namely, single-, two-, and three-signal analyses. In the single-signal analysis, we only consider ALL forcing signal as it includes all known forcings. In the two-signal analysis, we aim to partition the observations into responses to two external forcings, namely, anthropogenic (ANT) and natural (NAT) forcings. Here, the ANT response is estimated as the difference between ALL and NAT (i.e., ANT = ALL − NAT), assuming that the responses to ANT and NAT forcings are additive. In the three-signal analysis, we follow the method used in Hu et al. (2020) and the observed changes are regressed onto three signals, GHG, AA, and NAT. Moreover, we claim that the signals can be detected and separated in the two- and three-signal analyses, when the 90% ranges of their corresponding scaling factors are above zero.

3. Results

a. Observed changes in DTR

Figure 1 shows the length of observational record for DTR in each grid box and the number of available grid boxes for three observational datasets. For the CRU, there are stable data of DTR over the global land since 1901, which cover most of the land area except Antarctica. While CRU data have a good spatial coverage prior to the 1950s, values for many grid boxes were provided through data interpolation. For the Berkeley dataset, the number of grid boxes shows a step change around 1955, mainly due to the addition of the Antarctic continent data in recent decades, and it is slightly less than those of CRU in the rest of land. Further comparison shows that the grid boxes with data longer than 100 years are similarly located in Berkeley and CRU, suggesting a similar source of original station data. For the CLSAT, the available number of grid boxes shows a gradual increase before stabilizing around 1961, and then become more comparable to the other two observations. The early observations for this dataset are mainly located in North America, western Europe, Australia, and East Asia (Fig. 1a). There are fewer than 150 grid boxes where all three datasets have values in the first two decades (Fig. 1d). Thus, large differences exist in the changes of DTR during the early time period, especially at the continental scale, consistent with earlier findings.

Figure 2 shows time series of observed global average of DTR, Tmax, and Tmin anomalies (relative to 1961–90) computed from the three observational datasets based on all grid boxes of individual datasets. The time series of Tmax and Tmin resemble that of the global mean temperatures. The observed DTR has decreased for the period of 1901–2014, with a linear rate of -0.025°C decade^{-1}; the decrease mainly occurred during the 1950s to 1980s. The rapid decrease from the mid-1950s to the early 1980s is mainly due to the obviously more rapid increase of Tmin relative to that of Tmax during this period. In the early period of 1901–50, long-term changes in the DTR are small, and are similar across three datasets but there are some differences in the magnitude of variability between that in Berkeley and that in the other two datasets. The main reason is a relatively smaller Tmin during 1921–50 while Tmax values are similar across the datasets. This Tmin-induced difference in DTR is consistent with previous studies and may be due to the instability of Tmin observation during this period (Menne et al. 2012; Sun et al. 2018). During 1951–2014, CRU and CLSAT are more similar to each other while they appear to be slightly different from Berkeley. Again, the difference in Tmin in Berkeley is the main reason for the different changes of DTR for three datasets during this period. Overall, there is larger uncertainty for DTR changes in the early period but high consistency since the mid-1950s. The difference in Tmin among the dataset is the main source of the uncertainty.

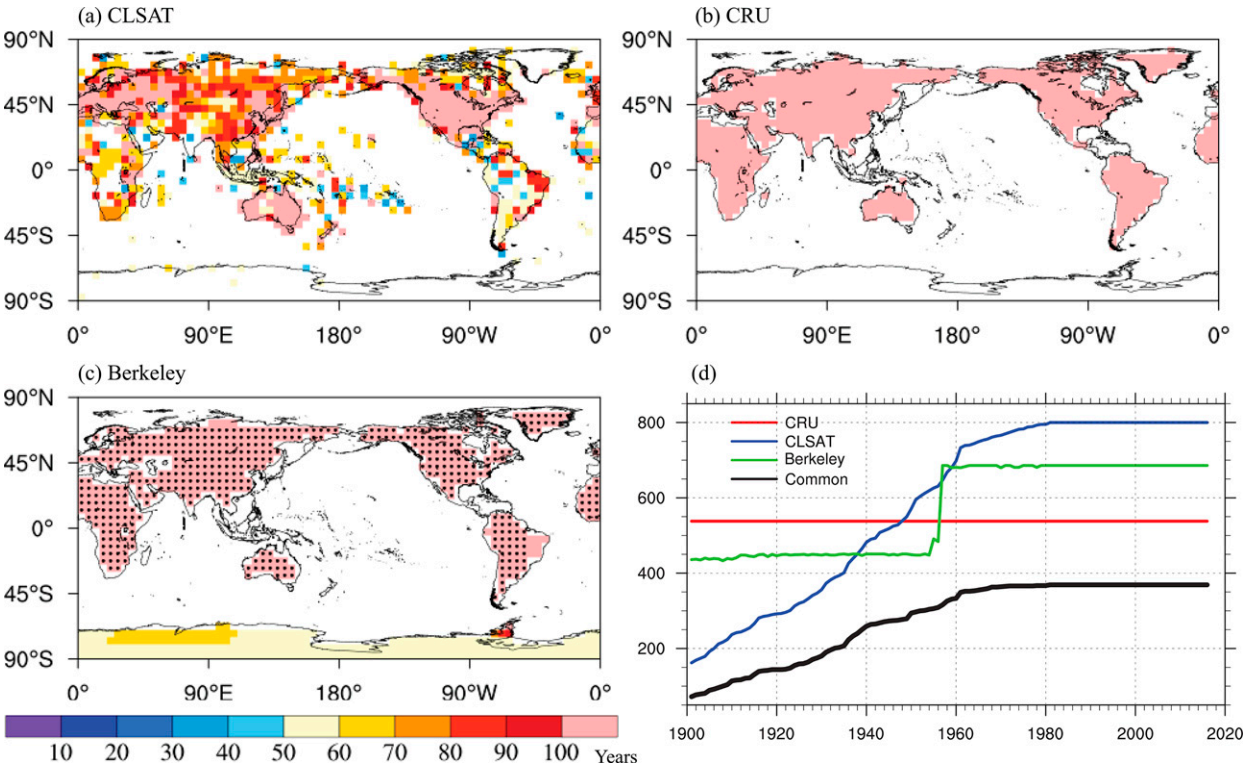

FIG. 1. Distribution of global land observations from 1901 to 2014. (a)–(c) Color points indicate the different record length in each grid box for the (a) CLSAT, (b) CRU, and (c) Berkeley data. A grid cell is marked with a black dot in (c) if both CRU and Berkeley datasets have observations over 100 years at this grid. (d) The number of available grid cells in different datasets over the global land; the thick black line indicates the number of grids common to all three data sources.

At continental scale and in China (Fig. 3; see also Figs. S1 and S2 in the online supplemental material), results are similar to the global mean but with larger uncertainties in a few continents. It is clear that the differences among three datasets are larger in ASI and SAM than in other continents in the early historical period, reflecting a large uncertainty of data in these areas. Again, differences of DTR in the three datasets are mainly caused by the difference in Tmin. In Asia and Europe, smaller Tmin in CLSAT corresponds to larger DTR during 1921–50. Note that there are very few grids in the three observation datasets in the early twentieth century in South America, which resulted in little comparability of DTR changes in different datasets during this period. This may hinder the detectability of the signal for this continent.

Given the similarity and the differences among the observational datasets mentioned above, in the following we will report the results based on the use of CRU data. We note that detection and attribution results for the period 1951–2014 are similar regardless of which observational dataset is used (see Figs. S3–S5 in the online supplemental material).

b. *Comparison of observed and simulated changes in DTR*

Figure 4 shows observed and model simulated linear trends of the DTR during two periods, 1901–2014 and 1951–2014. During 1901–2014, decreasing trends are observed in most areas of the world, but regional differences are also present. The large decreasing trend of DTR is seen over East Asia, North America, and Australia, which is mainly due to larger increase of Tmin than Tmax. The negative trends in parts of China and Canada can be as large as -0.12°C decade^{-1}, which means the DTR decrease of 1.37°C during 1901–2014. There are also small parts of western Europe, southern Africa, and Latin America showing very small positive changes. Larger increases in Tmax in these region may partially explain this difference, but more reliable data and further research are needed to understand the combination of mechanisms through which the change comes about. Figure 4c shows the multimodel ensemble mean trend of DTR under ALL forcing. The model simulated spatial pattern is generally consistent with the observations, which shows a decrease of DTR in most places. The observed increasing trends over southern Africa and Latin America are partially reproduced by the models, but the magnitude of trends is underestimated. The models could not reproduce the increasing trends in western Europe and central Asia. Figures 4e and 4g show the responses of DTR to GHG and AA forcings. The GHG trends are quite similar to those under ALL forcing but with weaker magnitude, indicating an important role of GHG forcing in the changes of DTR in the past century. The AA trends display the opposite changes to the observations in most land areas of the Northern Hemisphere, but similar

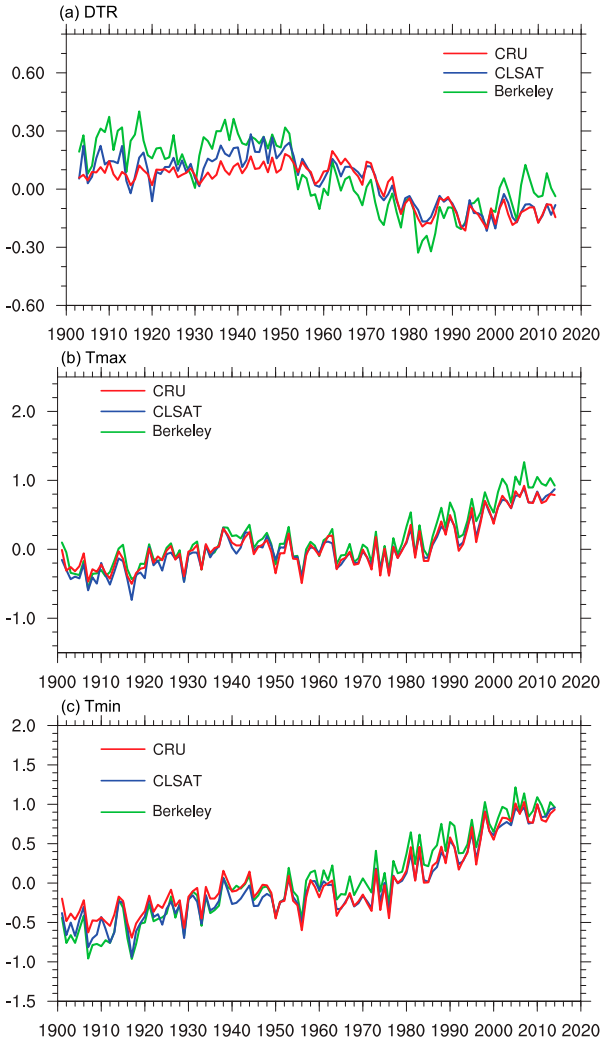

FIG. 2. Time series of global mean (a) DTR, (b) Tmax, and (c) Tmin anomalies (relative to 1961–90) based on observed data. The results are based on all grids of individual datasets.

changes in the AUS and SAM with much weaker magnitude. Over the northern high latitudes, the ensemble trend is mostly positive. This is different from the popular perception that aerosol must have been the main cause for DTR reduction. Figure 4i shows the trends in the multimodel ensemble mean under NAT forcing. The NAT trends are generally weak, much weaker than the observations for DTR, and in some regions (such as North America and southern Africa) the responses to NAT forcing are opposite to the observations, suggesting that NAT forcing alone cannot explain the observed changes in DTR.

The right column of Fig. 4 further compares observed and modeled DTR changes during the period of 1951–2014. It is apparent that the DTR during this period has decreased more rapidly than that during 1901–2014 for both observations and models, but the spatial patterns of trends are similar to those of longer period. In most areas of Eurasia, the decrease of DTR can be as large as −0.96°C over 1951–2014 (Fig. 4b), which is mainly due to larger warming of Tmin than the Tmax (Figs. S6 and S7 in the online supplemental material). For the models, the trends over 1951–2014 in the multimodel ensemble mean under ALL, GHG, AA, and NAT forcings exhibit similar characteristics to those in the period of 1901–2014. The models underestimate the decreasing trend in Eurasia and fail to reproduce the observed changes in Africa and South America (Fig. 4d), which may also indicate the problem arising from observational data availability and quality in those regions. The simulated changes in Tmax (Fig. S6) and Tmin (Fig. S7) lend the support to the changes in DTR. For example, in South America, the model overestimates the increasing trend of Tmax during 1951–2014, leading to an increasing trend in the simulated DTR, which is opposite to the observed results. These results indicate that the decrease of DTR during 1901–2014 was mainly due to the large decrease in DTR during 1951–2014, which is consistent with previous studies (Sun et al. 2018).

Figure 5 shows the global and continental mean temporal evolution of the 5-yr mean anomaly (relative to 1901–30) of DTR in the observations and simulations during 1901–2014. Changes in Tmax and Tmin are also shown in Figs. S8 and S9 in the online supplemental material. Globally, the observed Tmax, Tmin, and DTR are characterized by small changes in the early decades. During the period from the 1960s to early 1980s, an obvious decrease in DTR was observed as mentioned in the previous analyses and is mainly due to the significant increase of Tmin and smaller change in Tmax. Subsequently, the warming of Tmax is close to or slightly smaller than Tmin so the decrease of DTR has slowed down since the mid-1980s. At the continental (ASI, EUR, NAM) and national (China) scale, the DTR changes show clear regional differences. The observed DTR in ASI and EUR had an apparent increase from the 1930s to the 1960s, which was related to a more rapid increase of Tmax than Tmin, but the significance of these changes remains to be studied. On the global scale, the modeled response to ALL forcing generally reproduced the observed changes in Tmax, Tmin, and DTR, including almost no change in DTR prior to 1950s and a decrease after 1950. But there are also notable differences: the modeled response is a monotonic decrease but the observation showed a sharp decrease during the 1950s to 1980s and some recovery after the 1980s. Models also could not capture the large changes around the 1930s to 1980s in ASI and EUR. The model spread roughly covers the observed series. The responses to GHG show temporal variations similar to those under ALL forcing. The changes in the AA simulations are opposite to those in the observations and have a smaller magnitudes than the GHG responses. The NAT results show very little contribution to the DTR changes.

The linear trends of observed and model simulated Tmax, Tmin, and DTR during the period of 1901–2014, 1951–2014, and 1901–50 are further compared over the globe, five continents, and China (Fig. 6). During 1901–2014, the linear trends of observed Tmax and Tmin are close to the ALL results at the globe and Northern Hemisphere, as are the DTR changes. In SAM, there is no significant trend in DTR in the observations

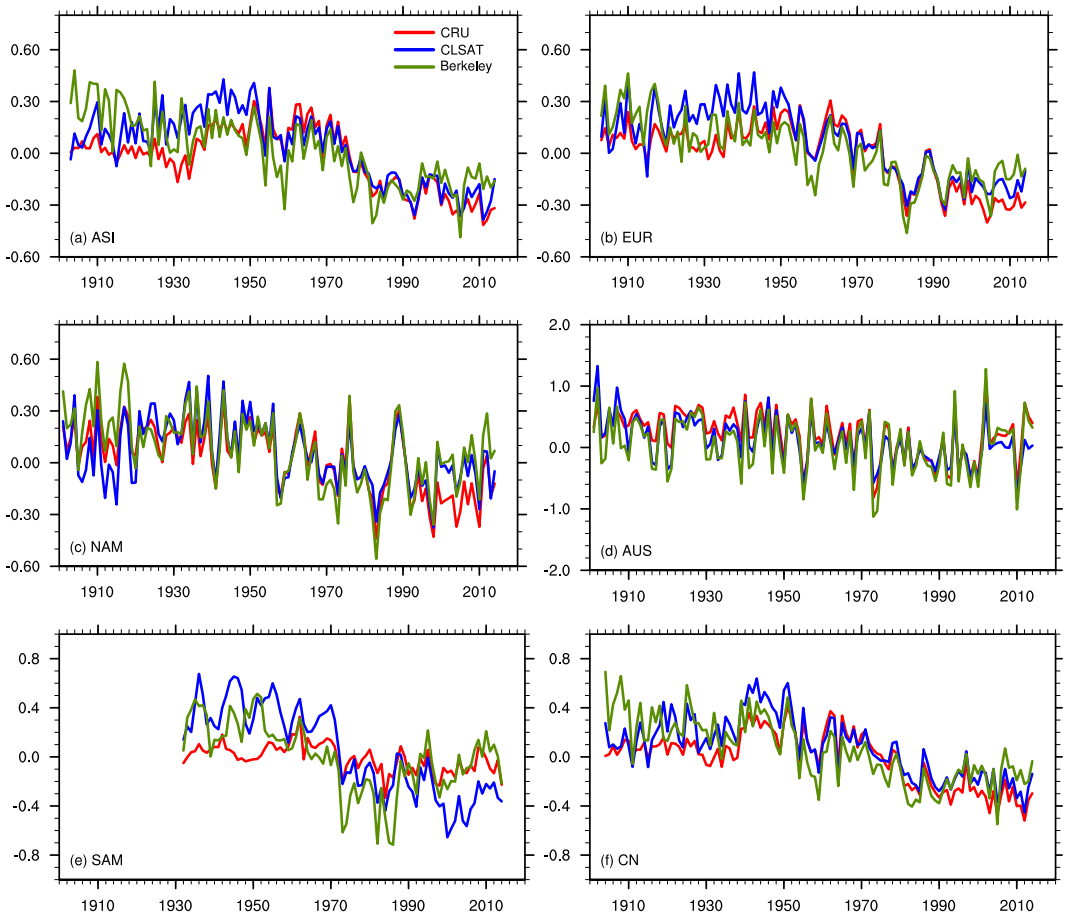

FIG. 3. Time series of regional mean DTR anomalies (relative to 1961–90) in (a) ASI, (b) EUR, (c) NAM, (d) AUS, (e) SAM, and (f) CN based on observed data. The results are based on all grids of individual datasets.

and model simulations, while in AUS the trends in Tmax and Tmin are very close in the models, which leads to very small trend in modeled DTR and is inconsistent with the real observations. During 1951–2014, changes in Tmax are smaller than those in Tmin in both observation and simulation. Thus, DTR (Tmax − Tmin) shows a decreasing trend. When the change of Tmax is overestimated while Tmin is not, the difference between changes in Tmax and Tmin becomes smaller (as Tmax < Tmin), which means the change of DTR is underestimated in the model results. Thus, the decrease trends of DTR in model results are smaller than those in observations during this period. During 1901–50, a slight increase of DTR can be found in most domains in the observations, while these features are not captured by the models. But observational data are quite uncertain too.

The observed and multimodel simulated power spectra of the DTR anomalies in different domains are shown in Fig. 7 (see also Figs. S10 and S11 in the online supplemental material for the power spectra results of Tmax and Tmin). We calculate the power spectra based on the regional mean time series over 1901–2014 from observations and separately from each simulation in the ALL and NAT experiments. The historical ALL simulations encompass the variability of the observations on all time scales examined in almost all cases, suggesting that the model simulations reasonably reproduce the observed DTR variability. Similar conclusions can be obtained from the Tmax and Tmin results (Figs. S10 and S11). Together with Fig. 5 and results of residual consistency, this gives us confidence that variability in the simulations is perhaps not too different from that in the observations.

c. *Detection results for Tmax and Tmin*

Figures 8 and 9 show the best estimates and the 90% confidence intervals of the scaling factors from the single-, two-, and three-signal detection analyses for the Tmax and Tmin during 1901–2014 and 1951–2014. During 1901–2014, the ALL and ANT signals can be robustly detected over global land and most continents for both Tmax and Tmin. The 90% confidence intervals of the scaling factors are all above zero and the residual consistency tests are passed in most cases. For the global series (single and combined), the 90% confidence intervals for ALL signal include 1, indicating that the observed changes in Tmax and Tmin are consistent with the expected response to the combined effect of anthropogenic and natural external forcings over the past century. It is worth pointing out that in almost all cases, the scaling factor for Tmax is

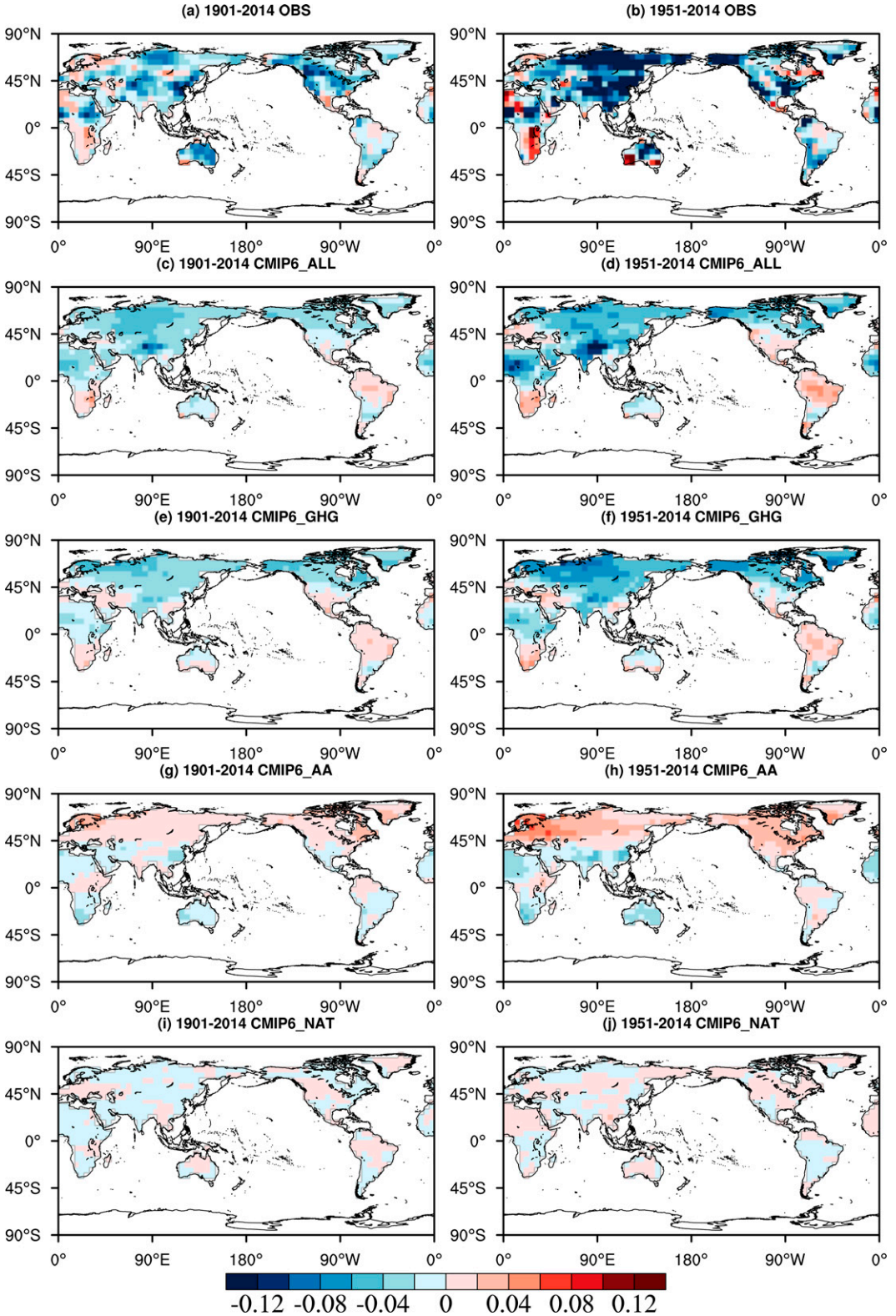

FIG. 4. Trends [°C (10 yr)$^{-1}$] in the annual DTR anomalies over (left) 1901–2014 and (right) 1951–2014 based on (a),(b) CRU observations and the model-simulated responses to the (c),(d) ALL; (e),(f) GHG; (g),(h) AA; and (i),(j) NAT forcings. White areas over the land indicate that there is no observation in that grid cell.

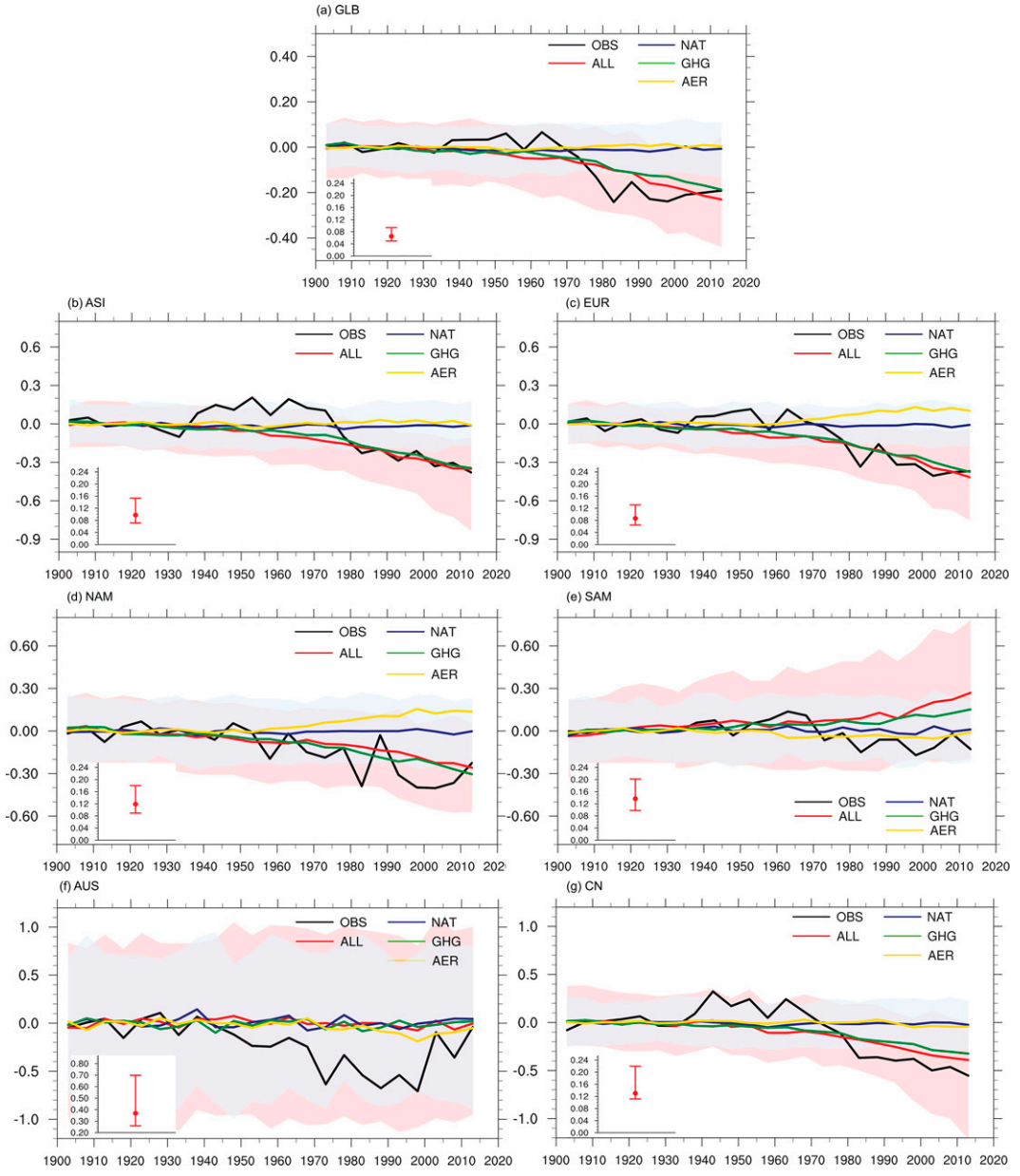

FIG. 5. Time series of 5-yr mean anomaly values (relative to 1901–1930) averaged over the (a) global, (b) Asian, (c) European, (d) North American, (e) South American, (f) Australian, and (g) Chinese land areas for DTR (°C) based on the CRU observations (black) and multimodel simulations under the ALL (red), NAT (blue), GHG (green), and AER (orange) forcings. Shadings show the 5%–95% ranges of the individual model simulations. The median value and 5%–95% range of variability estimated from control runs are shown as inset plots.

smaller than that for Tmin, indicating larger underestimation in the model-simulated Tmax response. The NAT can be detected in the global land (GLB) and the Northern Hemisphere domains for Tmax, which indicates the possible influence of volcanic and solar activities. In the three-signal analyses, the GHG and AA signals can be robustly detected and separated from each other in Tmax and Tmin over global land, four of the five continents, and China, with AUS being the exception. The NAT signal cannot be detected for most domains, suggesting that it cannot be distinguished from internal variability in the three-signal detections. These results indicate that when the three signals are taken into account together, both GHG and AA signals can be detected against the natural variability and thus play the dominant roles in the changes of Tmax and Tmin during the past century over global land and most continents.

For the period of 1951–2014 (Fig. 9), the ALL and ANT signals are robustly detected in Tmax and Tmin over almost

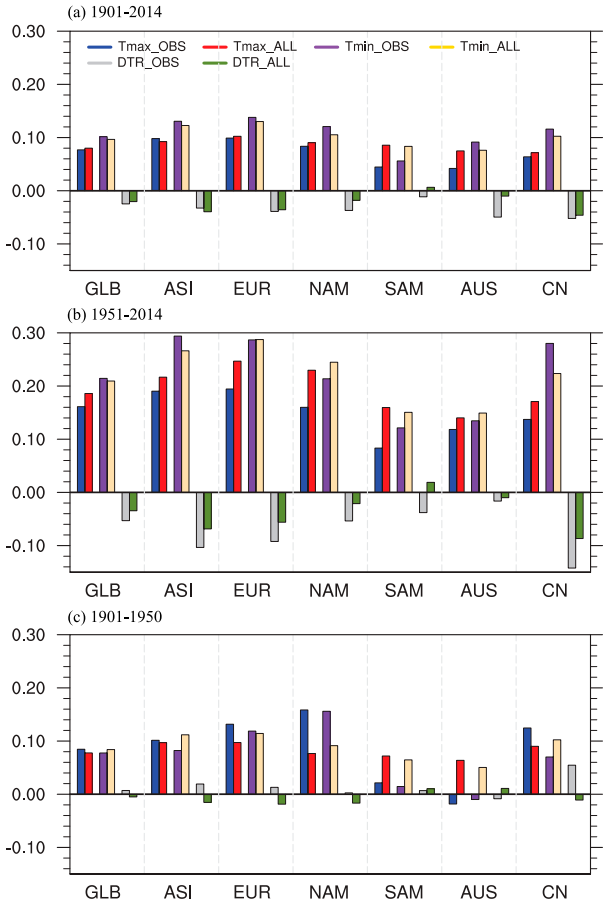

FIG. 6. The long-term trend [°C (10 yr)$^{-1}$] for time series of 5-yr mean anomaly values (relative to 1901–30) averaged over the global, continental, and Chinese land regions for Tmax, Tmin, and DTR over (a) 1901–2014, (b) 1951–2014, and (c) 1901–50. Observed and model results under ALL forcings are shown.

all domains, with the Tmin over AUS failing in the residual consistency tests. Note that the observed changes of Tmax are overestimated in the simulations under the combined effects of ANT and NAT external forcings, as the best estimates and 90% confidence intervals of scaling factors for ALL are below 1 in most domains. For Tmin, the simulated changes are generally consistent with the observations, as the 90% confidence intervals of scaling factors include 1 in most domains. The three-signal analyses exhibit that only the GHG signal can be robustly detected and separated in all domains except AUS, suggesting the dominant role of GHG in the observed changes over 1951–2014. As compared with the results for 1901–2014, the AA signal cannot be detected against noise in a shorter period of 1951–2014. A possible reason is a smaller decreasing trend of AA results in a shorter period and thus a weaker signal in comparison with a longer period of 1901–2014.

We further quantify the attributable changes from the GHG, AA, and NAT forcings to the observed Tmax and Tmin over the past century based on the corresponding scaling factors obtained in the three-signal analysis (Fig. 10). In all cases, the best estimate of the increase in Tmax and Tmin attributable to GHG forcing is larger than the observed changes, which is offset to a certain extent by the cooling effects of AA forcing. The NAT influences are very weak in all the domains. Globally, it is evaluated that the GHG forcing has increased Tmax and Tmin by 1.25°C (90% confidence intervals: 0.82°–1.69°C) and 1.41°C (0.95°–1.87°C), respectively, which has been offset 0.47°C (0.22°–0.77°C) and 0.36°C (0.11°–0.64°C), respectively, by AA forcing. The combined influence from external forcings has led to the changes of 0.78°C (0.68°–1.09°C) and 1.05°C (0.93°–1.39°C), respectively, over 1901–2014, which is very close to the observations. At continental scales and in China, the attribution results are similar to the global mean, with GHG being the main driver.

d. Detection results for DTR

Figure 11 shows the best estimates and the 90% confidence intervals of the scaling factors from the single- and two-signal detection analyses for the globe, three continents in the Northern Hemisphere, and China. In SAM and AUS, there is no significant trend over the past century and the models show poor performance in simulating most of the variation. We thus exclude the SAM and AUS regions in the detection analyses. For the period of 1901–2014, the scaling factors of ALL in all domains are significantly greater than zero at the 10% significance level. The models slightly underestimate the observed DTR because the best estimates of the scaling factors are greater than unity. The residual consistency tests failed. But when the model simulated variability is doubled (as has often been done in the past; e.g., Polson et al. 2013), the residual consistency passed in general and the 5th percentile of the scaling factor is still above zero, indicating that the detection is valid (Fig. 11b). From the two-signal detection, the 90% confidence intervals of the ANT scaling factors entirely lie above zero and the residual consistency tests passed in all domains, indicating that the ANT signal can be detected over the past century when the influence of NAT is taken into account. Note that the scaling factor for ANT signal is of similar magnitude to that of ALL, and is larger than unity in almost all cases, indicating the dominant influence of ANT forcing and the underestimate of DTR changes in CMIP6 simulations.

For the 1951–2014 series (Fig. 12), the ALL and ANT signals are robustly detected, as the 90% confidence intervals of the scaling factors all lie above zero and the residual consistency tests are all passed, with the ALL signal in CN being the exception. The scaling factors and their 90% confidence intervals are larger than those in 1901–2014, suggesting a larger underestimate of DTR decrease in recent decades. This is mainly related to a high value of observed DTR around the 1950s and the overestimate of Tmax in CMIP6 during this period, which we have discussed above. Similar to the results obtained over 1901–2014, the NAT signal cannot be detected. In the three-signal detections, all the signals cannot be detected in the DTR changes (not shown).

We further calculate the projected DTR changes under the SSP2–4.5 scenario simulated by six models. As we are not able to conduct detection and attribution for the continents of South America (SAM) and Australia (AUS), we do not

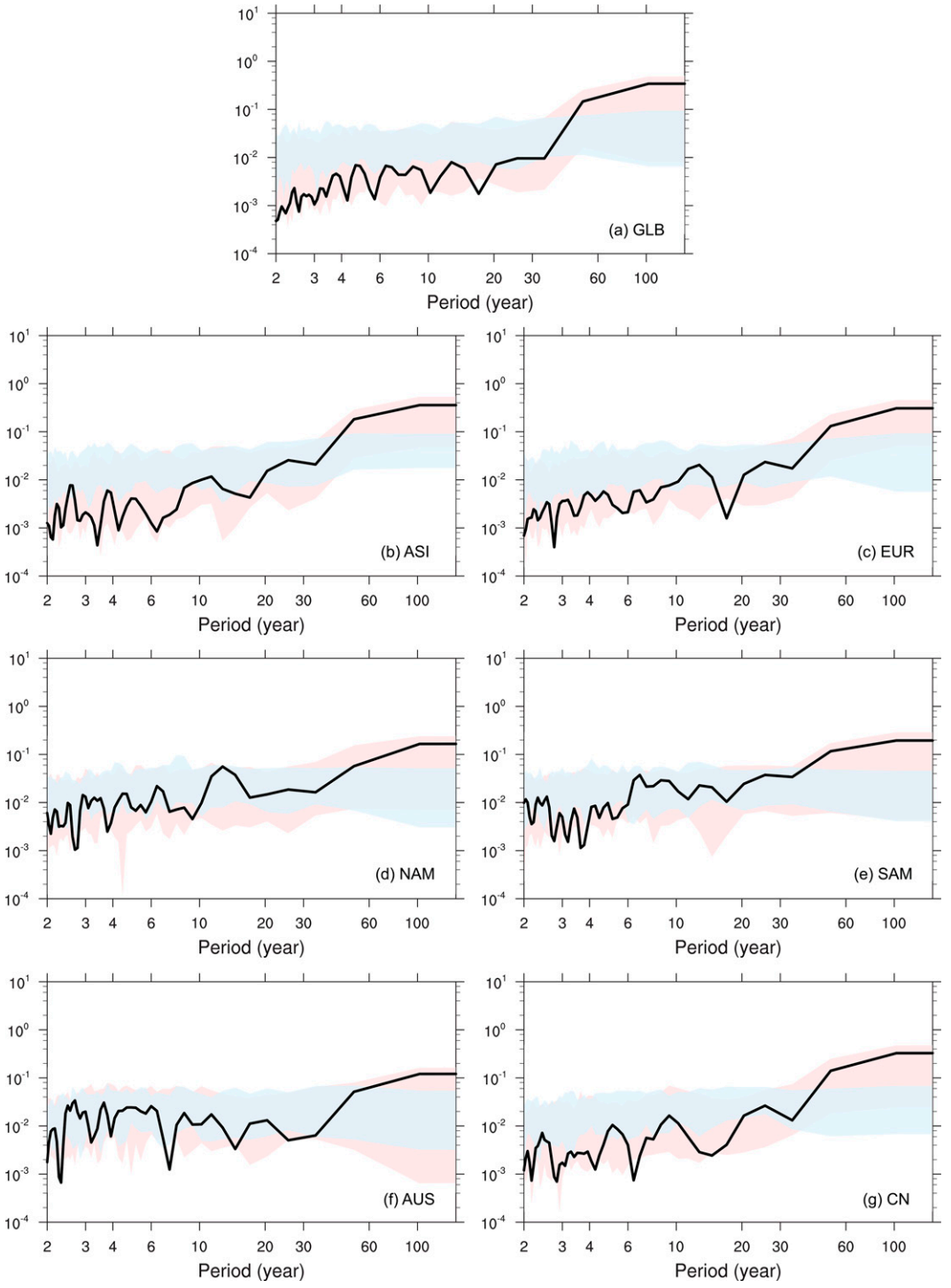

FIG. 7. Power spectral density of the DTR anomalies (relative to 1901–30) in the (a) global, (b) Asian, (c) European, (d) North American, (e) South American, (f) Australian, and (g) Chinese land regions from 1901 to 2014 for the observations (black) and model simulations. All model data have the same spatial coverage as the observations. The 5%–95% ranges of the ALL (pink) and NAT (blue) multimodel ensemble are shown as shaded areas.

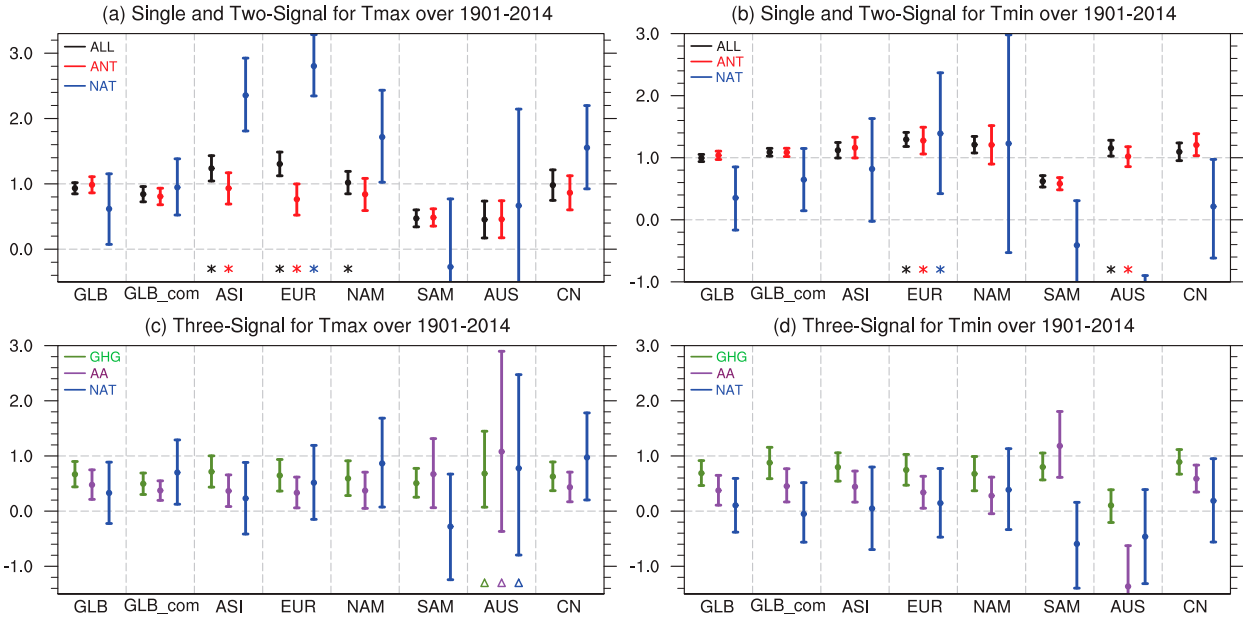

FIG. 8. Best estimates of the scaling factors and their 5%–95% uncertainty ranges for the 5-yr mean (left) Tmax and (right) Tmin anomalies during 1901–2014 based on (a),(b) single-signal (ALL), two-signal (ANT and NAT), and (c),(d) three-signal (GHG, AA, and NAT) analyses in global, continental, and Chinese land regions. The asterisks indicate failure of the consistency test because model-simulated variability is too low, and the triangles indicate failure of the consistency test because model-simulated variability is too high.

include SAM and AUS in the projection. In general, models project that the observed decrease in DTR will continue into the future over global land, northern continents, and China (Fig. S12 in the online supplemental material). We also found one paper that produced future projection based on CMIP5 simulations under the RCP8.5 scenario, which also showed a decrease in DTR in the future even though there could be large difference in the projections among the models (Lindvall and Svensson 2015). As aerosol is projected to decrease in both the SSP4.5 and RCP8.5 scenarios, the projected decrease in DTR must be a response to the increase in GHG, which is consistent with our detection and attribution results.

We also perform detection and attribution analysis over China based on the CN-2419 dataset during 1951–2014. The

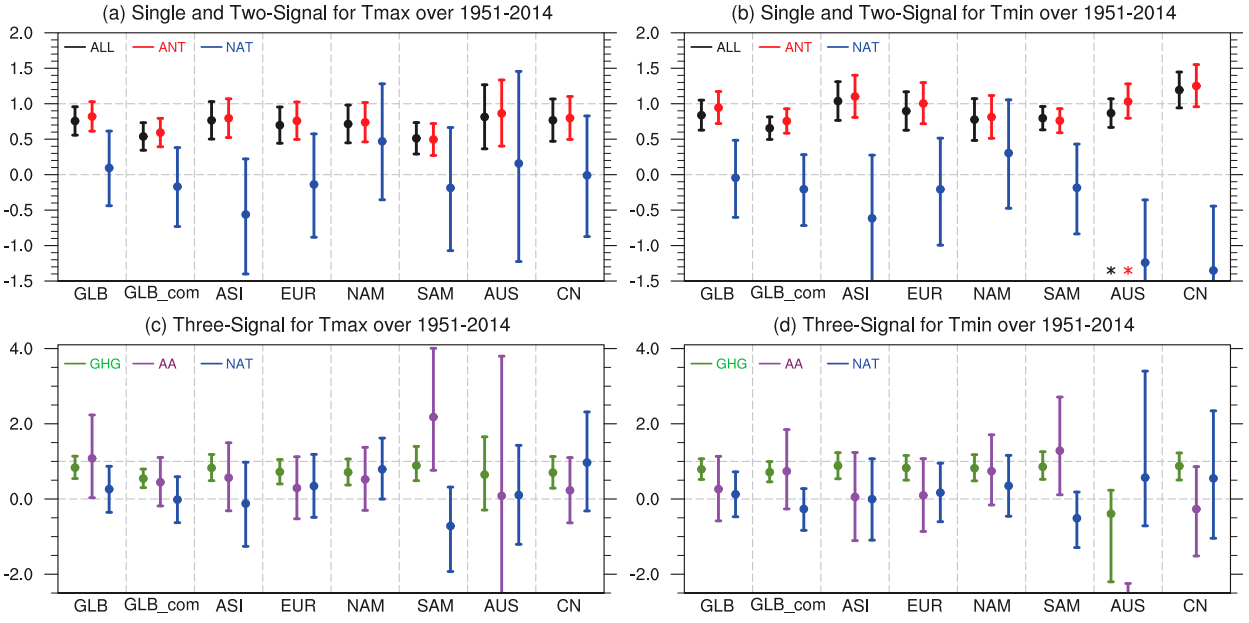

FIG. 9. As in Fig. 8, but for 1951–2014.

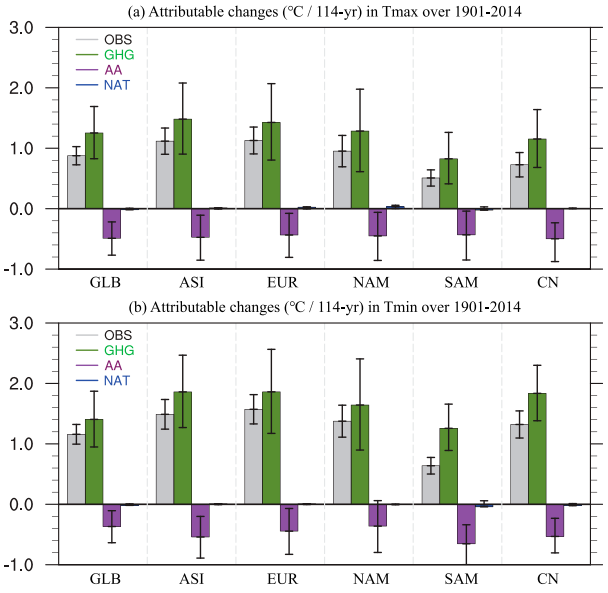

FIG. 10. Observed trends and trends attributable to GHG, AA, and NAT forcings in (a) Tmax and (b) Tmin over 1901–2014. The attributable trends are estimated as the linear least squares trends of the relevant time series multiplied by the corresponding scaling factors from the three-signal analyses in global, continental, and Chinese land regions.

results are very similar to those of analyses based on the CRU dataset. The time series of regional mean DTR anomalies computed from two different datasets (Fig. S13 in the online supplemental material) are very close to each other. The trend in CN-2419 is slightly stronger than that in CRU, and both of them are obviously larger than model simulations under ALL forcing. Further comparisons illustrate that the model show poor performance at China regional scale. The models underestimate the increasing trend of Tmin, but overestimate the increasing trend of Tmax in China (Fig. 6b), which caused the obviously smaller decreasing trend of DTR in simulations. Similar detection results in 1951–2014 are obtained from these two observations. The ANT signal is the dominant factor in the DTR changes over China in recent decades.

4. Conclusions and discussion

It is a challenge to quantify the human influence on long-term changes in DTR in the historical period. Our analysis uses the updated observations and multimodel ensemble data to conduct the detection and attribution analyses based on an optimal fingerprinting method. The larger datasets enable us to compare the difference of estimates for the simulated responses to external forcings and the internal climate variability, which are important for the robustness of detection and attribution analysis. The results show detectable influence of anthropogenic forcing on the DTR over the past century, supported by clear detection in Tmax and Tmin, as well as a high degree of consistency among the detection results based on different analysis settings.

We find robust evidence that anthropogenic influence is the main driver for the observed changes in Tmax and Tmin on global and continental scales and over China. Our analysis also provides clear evidence of decrease in DTR and its attribution to human induced climate change; the evidence is particular robust in the period 1951–2014 when the uncertainty in the observational DTR data is low and when the signal is also strong. The decrease in DTR in response to external forcing after the 1950s would have been comparable to what is in the observational record. Our century-scale analyses have a caveat,

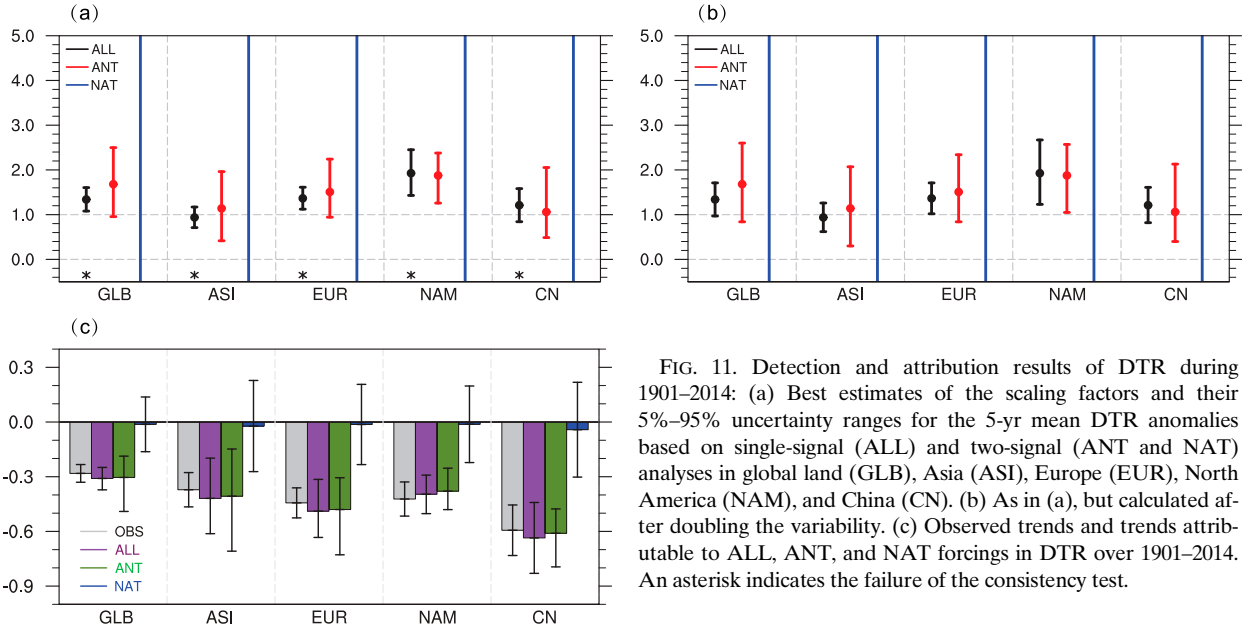

FIG. 11. Detection and attribution results of DTR during 1901–2014: (a) Best estimates of the scaling factors and their 5%–95% uncertainty ranges for the 5-yr mean DTR anomalies based on single-signal (ALL) and two-signal (ANT and NAT) analyses in global land (GLB), Asia (ASI), Europe (EUR), North America (NAM), and China (CN). (b) As in (a), but calculated after doubling the variability. (c) Observed trends and trends attributable to ALL, ANT, and NAT forcings in DTR over 1901–2014. An asterisk indicates the failure of the consistency test.

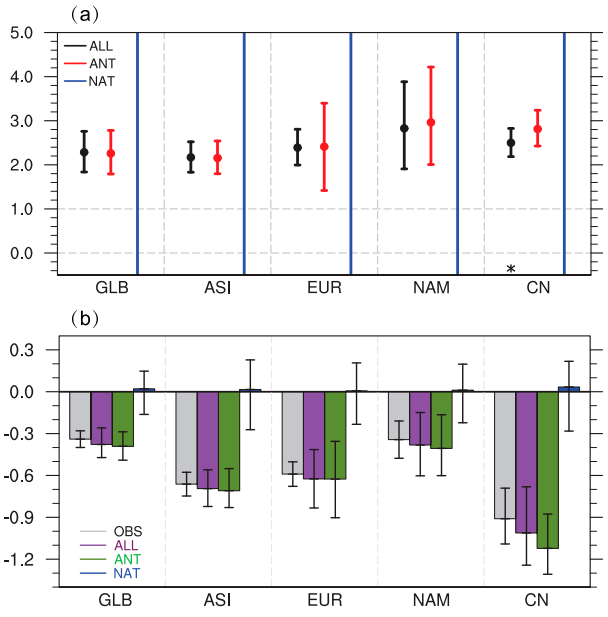

FIG. 12. Detection and attribution results of DTR during 1951–2014: (a) Best estimates of the scaling factors and their 5%–95% uncertainty ranges for the 5-yr mean DTR anomalies based on single-signal (ALL) and two-signal (ANT and NAT) analyses in global land (GLB), Asia (ASI), Europe (EUR), North America (NAM), and China (CN). (b) Observed trends and trends attributable to ALL, ANT, and NAT forcings in DTR over 1951–2014. An asterisk indicates the failure of the consistency test.

however, because DTR observations in the first half of the twentieth century are more uncertain. Since DTR is the difference between Tmax and Tmin, its response to external forcing is also the difference in the responses of Tmax and Tmin to external forcing. Thus, changes in DTR are expected to be smaller than changes in Tmax and Tmin, as shown in Fig. 5 and in Figs. S8 and S9 in the online supplemental material. Because DTR is the difference between Tmax and Tmin, its variability is the sum of variability in both Tmax and Tmin. With a much-reduced signal and larger variability, detecting a change in DTR is expected to be more difficult than that in Tmax or Tmin. Taking together, we conclude that it is unlikely there would have been detectable change in DTR prior to 1950s given the relatively small warming that occurred during that period. Given this conclusion and the robust attribution for the period since 1951 we can still conclude that human influence must have also resulted in a DTR increase on the century time scale despite the caveat in the century-scale analysis resulting from data issues in the early part of the twentieth century.

Acknowledgments. We acknowledge the Program for Climate Model Diagnosis and Intercomparison and the World Climate Research Programme's Working Group on Coupled Modeling for their roles in making the WCRP CMIP multimodel datasets available. This study was supported by the National Natural Science Foundation of China (42025503 and 41775082) and National Key R&D Program of China (2018YFA0605604).

Data availability statement. The CMIP6 model output is available online (https://esgf-index1.ceda.ac.uk/projects/cmip6-ceda/). The CRU (https://catalogue.ceda.ac.uk/uuid/3f8944800cc48e1cbc29a5ee12d8542d), Berkeley (http://berkeleyearth.org/data/), and CLSAT (http://climexp.knmi.nl/select.cgi?id=someone@somewhere&field=clsat_tmax) observational products are also all available online.

REFERENCES

Alexander, L. V., and Coauthors, 2006: Global observed changes in daily climate extremes of temperature and precipitation. *J. Geophys. Res.*, **111**, 1042–1063, https://doi.org/10.1029/2005JD006290.

Allen, M. R., and P. A. Stott, 2003: Estimating signal amplitudes in optimal fingerprinting part I: Theory. *Climate Dyn.*, **21**, 477–491, https://doi.org/10.1007/s00382-003-0313-9.

Bindoff, N. L., and Coauthors, 2013: Detection and attribution of climate change: From global to regional. *Climate Change 2013: The Physical Science Basis.* Cambridge University Press, 867–952.

Braganza, K., D. J. Karoly, and J. M. Arblaster, 2004: Diurnal temperature range as an index of global climate change during the twentieth century. *Geophys. Res. Lett.*, **31**, 405–407, https://doi.org/10.1029/2004GL019998.

Christidis, N., and P. A. Stott, 2016: Attribution analyses of temperature extremes using a set of 16 indices. *Wea. Climate Extremes*, **14**, 24–35, https://doi.org/10.1016/j.wace.2016.10.003.

Christy, J. R., W. B. Norris, and R. T. McNider, 2009: Surface temperature variations in East Africa and possible causes. *J. Climate*, **22**, 3342–3356, https://doi.org/10.1175/2008JCLI2726.1.

Dai, A., K. E. Trenberth, and T. R. Karl, 1999: Effects of clouds, soil moisture, precipitation, and water vapor on diurnal temperature range. *J. Climate*, **12**, 2451–2473, https://doi.org/10.1175/1520-0442(1999)012<2451:EOCSMP>2.0.CO;2.

Donat, M. G., and Coauthors, 2013: Updated analyses of temperature and precipitation extreme indices since the beginning of the twentieth century: The HadEX2 dataset. *J. Geophys. Res. Atmos.*, **118**, 2098–2118, https://doi.org/10.1002/jgrd.50150.

Easterling, D. R., and Coauthors, 1997: Maximum and minimum temperature trends for the globe. *Science*, **277**, 364–367, https://doi.org/10.1126/science.277.5324.364.

Eyring, V., and Coauthors, 2016: Overview of the Coupled Model Intercomparison Project phase 6 (CMIP6) experimental design and organization. *Geosci. Model Dev.*, **9**, 1937–1958, https://doi.org/10.5194/gmd-9-1937-2016.

——, and Coauthors, 2021: Human influence on the climate system. *Climate Change 2021: The Physical Science Basis*, Cambridge University Press, 423–552, https://www.ipcc.ch/report/ar6/wg1/downloads/report/IPCC_AR6_WGI_FullReport.pdf.

Gillett, N. P., and Coauthors, 2021: Constraining human contributions to observed warming since the pre-industrial period. *Nat. Climate Change*, **11**, 207–212, https://doi.org/10.1038/s41558-020-00965-9.

Harris, I., P. D. Jones, T. J. Osborn, and D. H. Lister, 2014: Updated high-resolution monthly grids of monthly climatic

observations: The CRU TS 3.10 dataset. *Int. J. Climatol.*, **34**, 623–642, https://doi.org/10.1002/joc.3711.

Hartman, D. L., and Coauthors, 2013: Observations: Atmosphere and surface. *Climate Change 2013: The Physical Science Basis*, T. F. Stocker et al., Eds., Cambridge University Press, 159–254, https://doi.org/10.1017/CBO9781107415324.008.

Hegerl, G. C., and Coauthors, 2007: Understanding and attributing climate change. *Climate Change 2007: The Physical Science Basis*, Cambridge University Press, 663–745.

——, and Coauthors, 2019: Causes of climate change over the historical record. *Environ. Res. Lett.*, **14**, 123006, https://doi.org/10.1088/1748-9326/ab4557.

Hu, T., and Coauthors, 2020: Human influence on frequency of temperature extremes. *Environ. Res. Lett.*, **15**, 064014, https://doi.org/10.1088/1748-9326/ab8497.

Jackson, L. S., and P. M. Forster, 2013: Modeled rapid adjustments in diurnal temperature range response to CO_2 and solar forcings. *J. Geophys. Res. Atmos.*, **118**, 2229–2240, https://doi.org/10.1002/jgrd.50243.

Jones, C. D., and Coauthors, 2011: The HadGEM2-ES implementation of CMIP5 centennial simulations. *Geosci. Model Dev.*, **4**, 543–570, https://doi.org/10.5194/gmd-4-543-2011.

Jones, G. S., P. A. Stott, and N. Christidis, 2013: Attribution of observed historical near-surface temperature variations to anthropogenic and natural causes using CMIP5 simulations. *J. Geophys. Res. Atmos.*, **118**, 4001–4024, https://doi.org/10.1002/jgrd.50239.

Karl, T. R., and Coauthors, 1993: A new perspective on recent global warming: Asymmetric trends of daily maximum and minimum temperature. *Bull. Amer. Meteor. Soc.*, **14**, 1007–1023, https://doi.org/10.1175/1520-0477(1993)074<1007:ANPORG>2.0.CO;2.

Kim, Y. H., and Coauthors, 2015: Attribution of extreme temperature changes during 1951–2010. *Climate Dyn.*, **46**, 1769–1782, https://doi.org/10.1007/s00382-015-2674-2.

Lewis, S. C., and D. J. Karoly, 2013: Evaluation of historical diurnal temperature range trends in CMIP5 models. *J. Climate*, **26**, 9077–9089, https://doi.org/10.1175/JCLI-D-13-00032.1.

Lindvall, J., and G. Svensson, 2015: The diurnal temperature range in the CMIP5 models. *Climate Dyn.*, **44**, 405–421, https://doi.org/10.1007/s00382-014-2144-2.

Liu, L., and Coauthors, 2016: The long-term trend in the diurnal temperature range over Asia and its natural and anthropogenic causes. *J. Geophys. Res. Atmos.*, **121**, 3519–3533, https://doi.org/10.1002/2015JD024549.

Lu, C., and Coauthors, 2016: Anthropogenic influence on the frequency of extreme temperatures in China. *Geophys. Res. Lett.*, **43**, 6511–6518, https://doi.org/10.1002/2016GL069296.

——, Y. Sun, and X. Zhang, 2018: Multimodel detection and attribution of changes in warm and cold spell durations. *Environ. Res. Lett.*, **13**, 074013, https://doi.org/10.1088/1748-9326/aacb3e.

McNider, R. T., and Coauthors, 2012: Response and sensitivity of the nocturnal boundary layer over land to added longwave radiative forcing. *J. Geophys. Res.*, **117**, D14106, https://doi.org/10.1029/2012JD017578.

Menne, M. J., and Coauthors, 2012: An overview of the Global Historical Climatology Network–Daily database. *J. Atmos. Oceanic Technol.*, **29**, 897–910, https://doi.org/10.1175/JTECH-D-11-00103.1.

Min, S. K., and Coauthors, 2013: Multi-model detection and attribution of extreme temperature changes. *J. Climate*, **26**, 7430–7451, https://doi.org/10.1175/JCLI-D-12-00551.1.

Mitchell, J. F. B., D. J. Karoly, G. C. Hegerl, F. E. Zwiers, and J. Marengo, 2001: Detection of climate change and attribution of causes. *Climate Change 2001: The Scientific Basis*, J. T. Houghton et al., Eds., Cambridge University Press, 695–738.

Morak, S., G. C. Hegerl, and N. Christidis, 2013: Detectable changes in the frequency of temperature extremes. *J. Climate*, **26**, 1561–1574, https://doi.org/10.1175/JCLI-D-11-00678.1.

Paaijmans, K. P., and Coauthors, 2010: Influence of climate on malaria transmission depends on daily temperature variation. *Proc. Natl. Acad. Sci. USA*, **107**, 15 135–15 139, https://doi.org/10.1073/pnas.1006422107.

Peng, S., and Coauthors, 2013: Asymmetric effects of daytime and night-time warming on Northern Hemisphere vegetation. *Nature*, **501**, 88–94, https://doi.org/10.1038/nature12434.

Polson, and Coauthors, 2013: Cause of robust seasonal land precipitation change. *J. Climate*, **26**, 6679–6697, https://doi.org/10.1175/JCLI-D-12-00474.1.

Ribes, A., and L. Terray, 2013: Application of regularised optimal fingerprint to attribution. Part II: Application to global near-surface temperature. *Climate Dyn.*, **41**, 2837–2853, https://doi.org/10.1007/s00382-013-1736-6.

——, S. Planton, and L. Terray, 2013: Application of regularized optimal fingerprinting to attribution. Part I: Method, properties and idealized analysis. *Climate Dyn.*, **41**, 2817–2836, https://doi.org/10.1007/s00382-013-1735-7.

Rohde, R., and Coauthors, 2012: A new estimate of the average Earth surface land temperature spanning 1753 to 2011. *Geoinfo. Geostat.*, **1**, 1, https://doi.org/10.4172/2327-4581.1000101.

——, and Coauthors, 2013: Berkeley Earth temperature averaging process. *Geoinfo. Geostat.*, **1**, 2, https://doi.org/10.4172/gigs.1000103.

Steeneveld, G. J., A. A. M. Holtslag, R. T. McNider, and R. A. Pielke, 2011: Screen level temperature increase due to higher atmospheric carbon dioxide in calm and windy nights revisited. *J. Geophys. Res.*, **116**, D02122, https://doi.org/10.1029/2010JD014612.

Stjern, C. W., and Coauthors, 2020: How aerosols and greenhouse gases influence the diurnal temperature range. *Atmos. Chem. Phys.*, **20**, 13 467–13 480, https://doi.org/10.5194/acp-20-13467-2020.

Stone, D. A., and A. J. Weaver, 2003: Factors contributing to diurnal temperature range trends in twentieth and twenty-first century simulations of the CCCma coupled model. *Climate Dyn.*, **20**, 435–445, https://doi.org/10.1007/s00382-002-0288-y.

Stott, P. A., 2003: Attribution of regional-scale temperature changes to anthropogenic and natural causes. *Geophys. Res. Lett.*, **30**, 1728, https://doi.org/10.1029/2003GL017324.

——, and Coauthors, 2001: Attribution of twentieth century temperature change to natural and anthropogenic causes. *Climate Dyn.*, **17** (1), 1–21, https://doi.org/10.1007/PL00007924.

——, and Coauthors, 2006: Observational constraints on past attributable warming and predictions of future global warming. *J. Climate*, **19**, 3055–3069, https://doi.org/10.1175/JCLI3802.1.

Sun, X., and Coauthors, 2018: Global diurnal temperature range (DTR) changes since 1901. *Climate Dyn.*, **52**, 3343–3356, https://doi.org/10.1007/s00382-018-4329-6.

Sunoj, V. S., P. V. Prasad, I. A. Ciampitti, and H. F. Maswada, 2020: Narrowing diurnal temperature amplitude alters carbon tradeoff and reduces growth in C4 crop sorghum. *Front. Plant Sci.*, **11**, 1262, https://doi.org/10.3389/fpls.2020.01262.

Tett, S. F. B., and Coauthors, 2002: Estimation of natural and anthropogenic contributions to twentieth century temperature

change. *J. Geophys. Res.*, **107**, 4306, https://doi.org/10.1029/2000JD000028.

Thorne, P. W., and Coauthors, 2016a: Reassessing changes in diurnal temperature range: A new dataset and characterization of data biases. *J. Geophys. Res. Atmos.*, **121**, 5115–5137, https://doi.org/10.1002/2015JD024583.

——, and Coauthors, 2016b: Reassessing changes in diurnal temperature range: Intercomparison and evaluation of existing global data set estimates. *J. Geophys. Res. Atmos.*, **121**, 5138–5158, https://doi.org/10.1002/2015JD024584.

Trenberth, K. E., and Coauthors, 2007: Observations: Surface and atmospheric climate change. *Climate Change 2007: The Physical Science Basis.* S. Solomon et al., Eds., Cambridge University Press, 235–336.

Wang, G., and M. E. Dillon, 2014: Recent geographic convergence in diurnal and annual temperature cycling flattens global thermal profiles. *Nat. Climate Change*, **4**, 988–992, https://doi.org/10.1038/nclimate2378.

Wang, K., and R. E. Dickinson, 2013: Contribution of solar radiation to decadal temperature variability over land. *Proc. Natl. Acad. Sci. USA*, **110**, 14 877–14 882, https://doi.org/10.1073/pnas.1311433110.

Xu, W., and Coauthors, 2013: Homogenization of Chinese daily surface air temperatures and analysis of trends in the extreme temperature indices. *J. Geophys. Res. Atmos.*, **118**, 9708–9720, https://doi.org/10.1002/jgrd.50791.

——, and Coauthors, 2018: A new integrated and homogenized global monthly land surface air temperature dataset for the period since 1900. *Climate Dyn.*, **50**, 2513–2536, https://doi.org/10.1007/s00382-017-3755-1.

Zhang, X., L. Alexander, G. C. Hegerl, P. Jones, A. Klein Tank, T. C. Peterson, B. Trewin, and F. W. Zwiers, 2011: Indices for monitoring changes in extremes based on daily temperature and precipitation data. *Wiley Interdiscip. Rev.: Climate Change*, **2**, 851–870, https://doi.org/10.1002/wcc.147.

——, R. W. Zwiers, and P. A. Stott, 2006: Multi-model multi-signal climate change detection at regional scale. *J. Climate*, **19**, 4294–4307, https://doi.org/10.1175/JCLI3851.1.

Zhou, L., R. E. Dickinson, A. Dai, and P. Dirmeyer, 2010: Detection and attribution of anthropogenic forcing to diurnal temperature range changes from 1950 to 1999: Comparing multi-model simulations with observations. *Climate Dyn.*, **35**, 1289–1307, https://doi.org/10.1007/s00382-009-0644-2.

Zwiers, F. W., and X. Zhang, 2003: Toward regional-scale climate change detection. *J. Climate*, **16**, 793–797, https://doi.org/10.1175/1520-0442(2003)016<0793:TRSCCD>2.0.CO;2.

——, ——, and Y. Feng, 2011: Anthropogenic influence on long return period daily temperature extremes at regional scales. *J. Climate*, **24**, 881–892, https://doi.org/10.1175/2010JCLI3908.1.